Archive of Applied Mechanics (2024) 94:1951–1966
https://doi.org/10.1007/s00419-024-02618-1

ORIGINAL

**MohammadAli Mesripoor · Mahdi Javanbakht · Hossein Jafarzadeh**

# Phase-field simulation of crack propagation in particulate nanocomposite materials considering surface stresses

Received: 10 August 2023 / Accepted: 7 May 2024 / Published online: 1 June 2024


**Abstract** This work studies crack propagation in particulate nanocomposites using the phase-field method. The crack propagation has been simulated in a wide range of loadings and the critical load for the crack growth has been obtained. Surface tension, as an inelastic stress, is introduced in the model in a thermodynamically consistent way. The effect of surface tension on the crack tip velocity and the crack evolution has been discussed. The finite element method via COMSOL multiphysics software has been utilized to solve the coupled phase-field and elasticity equations. Modeling and prediction of crack propagation for nanocomposites including different nanoparticles and under different loadings are the main purposes of this work. It is found that the kinetics and morphology of the crack propagation depend on the elastic moduli and the surface energy of nanoparticles as well as their longitudinal and angular distances to each other.

**Keywords** Phase-field · Double-well potential · Crack propagation · Nanoparticles · Surface stress

## 1 Introduction

### 1.1 Phase-field method

Several types of structural changes occur in materials, including fracture, dislocation evolution, phase transformation, grain growth, and twinning. The "sharp defect" approach is one method that can be used to model the mentioned changes. However, in the sharp defect approach, there is a jump in some parameters across interfaces or singularities near the crack tip. Notably, in numerical simulations, the numerical codes of the sharp defect method are significantly complicated and usually defined for three-dimensional (3D) conditions. Another method to study structural changes is the Phase-Field Method (PFM) which overcomes these drawbacks. A significant advantage of this method is that it can be used to anticipate and calculate the evolutionary course of nanostructures without requiring guesswork or predicting possible events and tracking interfaces. The phase-field method, as an intermediate between continuum approaches and atomistic methods, can obtain results at nano-dimensions and, at the same time, allows considering the size of samples and much larger solution times than atomistic analysis. Moreover, unlike classical thermodynamics, the PFM includes information about all initial, intermediate, and final states within each constituent phase as well as their respective interfaces. Hence, the phase-field approach can be viewed as a powerful method for modeling different structural changes, such as fracture [1–5], phase transformations [6–12], damage [13, 14], dislocation evolution [15], and twinning [16] as well as their interactions [17–20]. Surface stresses are incorporated in a few phase-field fracture models [5, 21, 22]. An order parameter is associated with each phase-field model, which is defined according to the discipline and introduced within the continuum mechanics framework. The present work

M. Mesripoor · M. Javanbakht (✉) · H. Jafarzadeh
Department of Mechanical Engineering, Isfahan University of Technology, Isfahan 8415683111, Iran
e-mail: javanbakht@iut.ac.ir

employs the PFM to continually split the domain of the samples into three parts as follows: the perfectly solid material ($\phi = 1$), the entirely damaged (broken) state ($\phi = 0$), and within each crack surface, which consists of a narrow thickness, the order parameter varies continuously between 0 and 1. The evolution of the crack order parameter occurs mainly in the crack tip zone. Therefore, in order to determine the evolution of the order parameter, the Ginzburg–Landau (GL) equation coupled with the set of elasticity equations, i.e., constitutive, kinematic, and equilibrium are utilized.

When it comes to the order parameter, all fracture phase-field models can generally be divided into two groups: first, those using a double-well potential, and second, the models using a single-well potential. The first phase-field model for fracture based on the GL phase transition was introduced in [1], where the order parameter was defined by means of the relative concentration of point defects in an amorphous material. Also, through the use of phase-field theory, the Karma–Kessler–Levine (KKL) model has been used to model mode III of crack propagation [2]. In contrast to the previous model [1], the KKL model overcame certain limitations and eliminated several nonphysical features, including the logarithmic dependence of the crack opening on the size of the system [2]. In this group of phase-field models, dynamic phenomena such as oscillating growth have been observed in crack growth [23]. A key feature of these models is the presence of a double-well potential that functions as the energy barrier in the phase transformation [23]. This KKL model was then extended to the modes I and II of fracture under the plane-strain conditions with the same double-well term [23] and also was generalized for the prediction of quasi-static crack paths in anisotropic brittle materials [24–26] and material heterogeneities [27]. There are some potentials with single-well energy in addition to phase-filed models with double-well potentials [28, 29]. Although these models have similarities with those previously described, several key differences exist between these two types. To extend Griffith's theory [30], variational formulations for fracture and associated phase-field models are studied in [31]. PFMs have been utilized in order to investigate various types of fracture, such as brittle [32], quasi-brittle [33], ductile [34] and fatigue crack propagation [35– 37]. Using single-well energy potentials eliminates some of the drawbacks associated with double-well potentials, including crack widening. Furthermore, a realistic stress–strain curve can also be obtained in this way [5]. However, they do not offer the flexibility necessary to present the complex shapes of stress–strain curves, such as those obtained from atomistic simulations.

### 1.2 Surface stresses

Considering the high surface-to-volume ratio at the nanoscale, surface effects can be incorporated into mechanical models to model fracture behaviors that are more realistic. Additionally, large surface stresses are present at sharp crack tips and sharp corners. All systems strive to minimize their energy, which affects how the crack nucleation and propagation behave. A theoretical study has demonstrated that when the surface stresses are greater than the elastic stresses in soft elastic materials, the energy release rate can be negative, i.e., cracks may even heal due to surface stresses [38]. A well-known fact is that on any material interface or surface, there are isotropic biaxial stresses acting with the force per unit length, $T$ [39]. The magnitude of the force per unit length is equal to the surface energy for liquid–gas and liquid–liquid interfaces $T = \gamma$. For these interfaces, elastic stresses are not supported, and the surface stresses are independent of strain. There is a resulting substantial increase in the normal stresses across the interface with the magnitude of $2\gamma/r$, where $r$ is the mean interface radius. However, surface stresses at an interface or a solid surface have a strain-dependent component that can be both compressive and tensile and is related to the elasticity of the surface.

In Griffith's crack propagation criterion, the surface energy is used as the basis and the surface stresses are not taken into account. A sharp crack tip and sharp corners, however, are subjected to surface stresses that are not negligible. It is difficult to measure surface stresses, which limits the number of quantitative predictions that can be made regarding how surface stresses affect crack propagation. In the sharp surface approach, the surface stress tensor, which has a dimension of force per unit length, is related to the surface energy by the equation $\bar{\sigma}_s = \gamma \boldsymbol{I}_s + \partial\gamma/\partial\boldsymbol{\varepsilon}_s$, where $\boldsymbol{I}_s$ is a two-dimensional surface unit tensor and $\boldsymbol{\varepsilon}_s$ is the surface strain [40]. The first and second terms of this equation are the residual surface stress and the deformation-dependent part of the surface stress, respectively. In most cases, this equation is utilized to include the effect of the surface stresses on the behavior of the crack propagation [41] by using the linear constitutive law $\partial\gamma/\partial\boldsymbol{\varepsilon}_s = \boldsymbol{C}_s : \boldsymbol{\varepsilon}_s$. Here, $\boldsymbol{C}_s$ is the fourth-order surface elastic moduli tensor. In the small strain theory [42], the elastic (first) part of the surface stress can be neglected since atomistic simulations demonstrate that the components of $\boldsymbol{C}_s$ are similar to $\gamma$ in the order of magnitude [41]. Additionally, the material parameters that determine the surface stresses are not well understood. A theoretical study was conducted on the surface stress in [43] as a

line force acting on the cleavage surface, whose effect was examined for the sharp crack tip with regard to the stress intensity factor. Based on the analysis of an elliptic void with surface elasticity, it was concluded that it was surface stresses that were responsible for the decrease in the applied stress intensity factor [44]. In this regard, several studies have been conducted for modes I [45, 46], II [47], III [45, 48], and mixed mode [41] by utilizing the theory of surface elasticity. The curvature radius of the crack tip plays a vital role in determining the deformation-dependent portion (second term) of the surface stress. The curvature radius of the crack tip has a significant influence on the stress magnitude and also changes the type of deformation from stretching to compression as well [49]. In the present study, the surface tensions are applied to the desired model.

### 1.3 Nanocomposite effect

It is demonstrated in [50] that in loaded polymer materials, microvoids and microcracks lead to the initiation and growth of cracks. The formation of microvoids and microcracks becomes more apparent by their coalescence as the loading progresses, resulting in cracks. The phase-field method has been widely used to track crack propagation in nanocomposites. A PFM was developed to anticipate the fracture toughness and tensile strength of clay-epoxy nanocomposites [51]. Also, this model was utilized to determine how surface energy is created during fracture in nanocomposites. Further, by taking the interphase zones between clay and the polymer matrix into account, the authors developed their model for clay-epoxy nanocomposites, which involved modeling clay particles as linear elastic materials that are embedded in a hyperplastic matrix [52]. A neural network algorithm was recently introduced to model crack propagation in brittle materials by minimizing the system's vibrational energy based on the phase-field theory [53, 54]. Based on the simulation results, it is indicated that crack paths anticipated by the introduced approach are consistent with literature reports. To investigate the rate-dependent fracture in solids, several formulations have been derived based on the phase-field approach [55, 56]. A rate-dependent model was proposed in [57] for materials made of rubber and based on PFM. The parameters needed in this model were identified and determined by using double-edge tensile and uniaxial tensile tests. Further, it has been found that interactions between nanofillers and polymer matrices as well as microstructural complexity affect the damage evolution in thermosetting polymer nanocomposites [58]. Initially, a composite material seems to be elastic, orthotropic, and linear, however, the situation becomes considerably more complex when material damage or failure occurs [58]. There have been numerous numerical approaches proposed over the recent years that have been used in order to model the nucleation and growth of cracks in composite laminates. Generally, crack models are categorized into two types: first, discrete crack models in which singular elements and a sharp crack topology are combined with each other in the classic finite element method [59, 60]. In this group of models, singularities appear due to the sharp crack topology [61]. Second, smeared crack models, unlike the first group models, do not meet conventional singularities. This advantage arises from the crack phase-field introduced in smeared crack models in order to simulate sharp cracks in the diffusive zone [51]. Newly, a cohesive zone model and a phase-filed model were proposed to simulate interface failure and brittle fracture, respectively, in complex laminates [62]. A multi-phase-field approach for crack propagation considering the contribution of the interface energy is recently presented which captures the intergranular and transgranular fracture [63].

In the present study, a particulate nanocomposite model in two-dimensional space is presented. The phase-field approach is utilized to model and predict the crack growth in a random distribution of nanoparticles in matrix. The effects of the Ginzburg-Landau equation, key parameters, such as the elastic moduli and the surface energy of matrix and nanoparticles, were investigated on the crack propagation.

This paper is organized as follows. In Sect. 2, the formulation of the model is presented. Section 3 presents the numerical procedure. Then, the effects of nanoparticles on the mechanical properties are discussed in Sect. 4. Finally, the verification of the given model has been approved.

## 2 Model

The formulation is based on small strains, i.e., the kinematic is governed by $\boldsymbol{\varepsilon} = \frac{1}{2}\left(\nabla \boldsymbol{u} + \nabla \boldsymbol{u}^T\right)$.

### 2.1 Laws of thermodynamics

An arbitrary volume $V$, which is continuous and consists of some cracks and surfaces, can be described using the laws of thermodynamics. In other words, each of the mentioned surfaces represents a narrow region within the volume, in which the order parameter varies sharply. The local form of the first and the second laws of thermodynamics can be derived using the equation of Cauchy stress for the traction vector $T_i = \sigma_{ij} n_j$, the theory of Gauss's divergence, the principle of material objectivity, and mass conservation in Eqs. (1) and (2), respectively:

$$\boldsymbol{\sigma} : \dot{\boldsymbol{\varepsilon}} - \rho \dot{U} - \nabla \cdot \boldsymbol{h} + \rho r + \nabla \cdot \left( \boldsymbol{G} \dot{\phi} \right) = 0 \tag{1}$$

$$\rho \theta \dot{s} - \rho r + \nabla \cdot \boldsymbol{h} - \frac{\nabla \theta}{\theta} \cdot \boldsymbol{h} \geq 0 \tag{2}$$

where $\rho$ is the material density, $\boldsymbol{h}$ is the heat flux vector, and $r$ is the input heat rate per mass unit. Here, $\boldsymbol{G}$ is a vector that represents the generalized surface forces conjugated to $\dot{\phi}$, $\theta$ is the temperature, and $s$ is the specific entropy. There are some terms of energy on the crack surface as a result of the dependency of the energy on the gradient terms. It is impossible for the global form of the thermodynamic laws to be applied on an arbitrary volume without considering the generalized force, and also, there cannot be a decisive transition from global to local form. This problem can be resolved by adding the generalized surface forces without compromising the boundary conditions. By considering the laws of thermodynamics and by substituting Eq. (1) into Eq. (2), another form of dissipation inequality can be obtained as follows.

$$\rho D_{tot} := \boldsymbol{\sigma} : \dot{\boldsymbol{\varepsilon}} - \rho \dot{U} + \rho \theta \dot{s} + \nabla \cdot (\boldsymbol{G} \phi) - \frac{\nabla \theta}{\theta} \cdot \boldsymbol{h} \geq 0 \tag{3}$$

The free energy can also be formulated in terms of the temperature and the strain in order to omit $\dot{s}$ from the formulation. Therefore, the Helmholtz free energy per mass unit is introduced as:

$$\psi = U - s\theta \tag{4}$$

Hence, Eq. (3) can be rewritten and split into two parts in Eqs. (5) to (7) as:

$$\rho D_{tot} := \boldsymbol{\sigma} : \dot{\boldsymbol{\varepsilon}} - \rho \dot{\psi} - \rho \dot{\theta} s + \nabla \cdot \left( \boldsymbol{G} \dot{\phi} \right) - \frac{\nabla \theta}{\theta} \cdot h \geq 0 \tag{5}$$

$$\rho D_{mech} = \boldsymbol{\sigma} : \dot{\boldsymbol{\varepsilon}} - \rho \dot{\psi} - \rho \theta \dot{s} + \nabla \cdot (\boldsymbol{G} \dot{\phi}) \geq 0 \tag{6}$$

$$\rho D_{ther} = -\frac{\nabla \theta}{\theta} \cdot h \geq 0 \tag{7}$$

where $D_{mech}$ and $D_{ther}$ are called mechanical and the thermal dissipation, respectively. It is the former that refers to the material irreversibility, whereas the latter is related to the irreversibility, which is because of the presence of the temperature gradient.

Assuming that the energy is considered in the form of $\psi = \psi(\varepsilon, \phi, \nabla\phi, \theta)$ and then by substituting it to the inequality of dissipation, Eq. (6), the required equations can be obtained as

$$\boldsymbol{\sigma} = \rho \frac{\partial \psi}{\partial \boldsymbol{\varepsilon}} \tag{8}$$

$$\boldsymbol{G} = \rho \frac{\partial \psi}{\partial \nabla \phi} \tag{9}$$

$$\rho D_{mech} = \chi \dot{\phi} \geq 0; \quad \chi = -\rho \frac{\partial \psi}{\partial \phi} + \nabla \cdot \left( \rho \frac{\partial \psi}{\partial \nabla \phi} \right) \tag{10}$$

which are the constitutive law, the generalized force, and the mechanical dissipation, respectively. Also, in Eq. (10), $\chi$ is presented as the Ginzburg-Landau (GL) driving force. The detailed derivations on the equations of Eqs. (9–11) can be found in [5].

Further, as for the boundary conditions, it is necessary to prescribe the order parameter at the boundaries. This is similar to the approach, which can be used to prescribe the heat flux and the temperature as possible boundary conditions for the problem of heat conduction. The boundary condition is as follows.

$$\boldsymbol{n} \cdot \boldsymbol{G} = \boldsymbol{n} \cdot \rho \frac{\partial \psi}{\partial \nabla \phi} \tag{11}$$

where $\boldsymbol{n}$ is a vector perpendicular to the boundary. As one of the main advantages of the phase-field method, boundary domains are not required to be updated and tracked during fracture and growth of the crack. It is because of the order parameter which describes diffuse surfaces and varies between 0 for the crack and 1 for the perfectly solid material.

Here, the crack growth is regarded as a solid–gas phase transformation leading to a double-well free energy. The GL free energy is

$$\rho\psi = \frac{1}{2} I(\phi)\boldsymbol{\varepsilon} : \boldsymbol{C}_0 : \boldsymbol{\varepsilon} + A\phi^2(1-\phi)^2 + \frac{\beta}{2}|\nabla\phi|^2 \tag{12}$$

which consists of three parts: degraded elastic energy, double-well potential and the nonlocal gradient energy ($\Psi^{\nabla}$), respectively.

The degradation function $I(\phi) = 4\phi^3 - 3\phi^4$ describes a smooth change in the elastic modulus from its original constant value in the intact material,$\boldsymbol{C}_0$, to zero at the surface. Here, $A$ represents the height of the double-well barrier, which is related to the fracture energy and $\beta$ is the gradient coefficient. The double-well potential is used here for easier and more straightforward introducing surface stresses [5, 21, 22].

## 2.2 Evolution equation

By combining Eqs. (8) and (12) the stress tensor can be achieved as [21]

$$\boldsymbol{\sigma} = \rho\left(\frac{\partial}{\partial\boldsymbol{\varepsilon}}\left(\frac{1}{\rho}\left(\Psi^e + \Psi_d + \Psi^{\nabla}\right)\right) - \frac{\partial\left(\frac{\Psi^{\nabla}}{\rho}\right)}{\partial\nabla\phi} \otimes \nabla\phi\right) \tag{13}$$

The total stress tensor introduced in Eq. (19) can be decomposed into two parts of elastic and surface stress tensors. These two parts are presented below

$$\begin{aligned} \boldsymbol{\sigma}_e &= \frac{\partial\Psi^e}{\partial\boldsymbol{\varepsilon}} = \left(4\phi^3 - 3\phi^4\right)\boldsymbol{C}_0 : \boldsymbol{\varepsilon} \\ \boldsymbol{\sigma}_{st} &= \left(\Psi_d + \Psi^{\nabla}\right)\boldsymbol{I} - \beta\nabla\phi \otimes \nabla\phi \end{aligned} \tag{14}$$

Further, a linear relation between the order parameter variation rate ($\dot{\phi}$) and the thermodynamic driving force ($\chi$) can be accepted.

$$\chi = -\rho\frac{\partial\psi}{\partial\phi} + \nabla\cdot\left(\rho\frac{\partial\psi}{\partial\nabla\phi}\right) = -\rho\frac{\partial\psi}{\partial\phi} + \beta\nabla^2\phi \tag{15}$$

$$\dot{\phi} = L\chi = L\left(-\rho\frac{\partial\psi}{\partial\phi} + \beta\nabla^2\phi\right) = L(-6\phi^2(1-\phi)\boldsymbol{\varepsilon} : \boldsymbol{C}_0 : \boldsymbol{\varepsilon} - 4A\phi(1-\phi)(0.5-\phi) + \beta\nabla^2\phi) \tag{16}$$

$L$ is defined as the kinetic coefficient by assuming the crack under tensile stresses. Here, we do not distinguish between tensile and compressive stresses, because we just study mode I loading. Different approaches can be employed in order to prevent fracture under closing (compressive) stresses [5].

The profile of the crack surface can be explicitly determined by the solution GL equation in one-dimension [16]

$$\phi_s = \left(1 + e^{-\frac{x}{w}}\right)^{-1} \tag{17}$$

where $\omega := \sqrt{\beta/2A}$ is defined as the crack surface width. The subscript "$s$" for the surface refers to the localization at the diffused surface. Considering the definition of the surface energy which is the strain-independent part of the free energy, $\gamma$ can be related to $\beta$ and $\omega$ as below and the detailed derivation can be found in [21].

$$\gamma = \int_{-\infty}^{\infty}\left(A\phi_s^2(1-\phi_s)^2 + \frac{\beta}{2}|\nabla\phi_s|^2\right)\mathrm{d}x$$

$$= \int_{-\infty}^{\infty} \left(A\phi_s^2(1-\phi_s)^2 + A\phi_s^2(1-\phi_s)^2\right)\mathrm{d}x$$

$$= \int_{-\infty}^{\infty} \left(2A\phi_s^2(1-\phi_s)^2\right)\frac{\mathrm{d}x}{\mathrm{d}\phi_s}\mathrm{d}x = \sqrt{2A\beta}\int_0^1 A\phi_s(1-\phi_s)\mathrm{d}\phi_s = \frac{\beta}{6\omega} \tag{18}$$

By removing the parameters $A$ and $\beta$ in Eq. (18), and since $\omega = \sqrt{\beta/2A}$, the set of phase-field equations are obtained as [16]:

- The GL equation:

$$\frac{1}{L}\dot{\phi} = 6\phi^2(1-\phi)\boldsymbol{\varepsilon} : \boldsymbol{C}_0 : \boldsymbol{\varepsilon} + \frac{6\gamma}{\omega}\left(\omega^2\nabla^2\phi - \phi(1-\phi)(0.5-\phi)\right) \tag{19}$$

- The GL free energy:

$$\rho\psi = \frac{1}{2}(4\phi^3 - 3\phi^4)\boldsymbol{\varepsilon} : \boldsymbol{C}_0 : \boldsymbol{\varepsilon} + \frac{3\gamma}{\omega}\left(\phi^2(1-\phi)^2 + \omega^2|\nabla\phi|^2\right) \tag{20}$$

- The surface tension:

$$\sigma_{st} = \frac{6\gamma}{\omega}\frac{1}{\left(1+e^{-\frac{x}{\omega}}\right)^2\left(1+e^{\frac{x}{\omega}}\right)^2} \tag{21}$$

## 3 Numerical procedure

The equations in Sect. 2 is utilized to form the main structure of defined model based on the potential function of the characteristic parameter of the double-well potential. Numerical procedure and the simulation of crack growth was carried out in COMSOL Multiphysics software, and the segregation solver was utilized.

Mathematical and structural applications have been used to solve the problem. A rectangular $50 \times 60$ nm$^2$ sample is considered. Due to the symmetry in the geometry and loading of the sample, only half of it has been modeled to include the elasticity couple and the phase-field equation in it and reduce the computational time and effort. The displacement loading increases by rate of 1.5nm/ps up to 2 ps and then stay constant to the lateral edges. Figure 1 represents the sample schematic, boundary conditions and loading.

Initial crack is applied to the upper edge, the boundary condition of upper edge is a roller, and the lower edge is free. The whole process time is 10 ps. The finite element method with free tetrahedral refined mesh has been adopted with the size of minimum 9 to 12 pm. The plane-strain condition is considered.

Length, time and stress dimensions were normalized by 1 nm, 1 ps and 1 GPa, respectively.

Due to implementing the surface tensions, the initial shape of the crack will have a significant impact on numerical procedure. Sharp cracks cause singularity and heterogeneity in the process due to stress concentration near the sharp tip of the crack and especially in the presence of surface tensions. To prevent such singularity, the primary crack is introduced by phase-field using the polynomial hyperbolic function of Eq. 22 based on Eq. 21.

$$\phi = 0.99 - \begin{cases} \left(1+e^{\frac{x-10\omega}{\omega}}\right)^{-1} & y > 50\text{ nm} - 10\omega \\ \left(1+e^{\frac{x-10\omega}{\omega}}\right)^{-1} \times \left(1+e^{(y-(50-10\omega))/\omega}\right)^{-1} & y \le 50\text{ nm} - 10\omega \end{cases} \tag{22}$$

Material and mechanical properties of the used matrix and particle sample material are defined as below in Table 1, unless stated otherwise.

In the solid ($\phi = 1$) or gas ($\phi = 0$) states the derivative of energy with respect to the order parameter is zero ($\partial\Psi/\partial\phi = 0$). Hence, the initial order parameter of $\phi = 0.99$ is considered for the intact solid. The elastic energy of the gas phase is practically equal to zero. However, to prevent the numerical challenges from diverging, a very small elastic energy is assigned to the gas phase (crack) and the effects of this value are

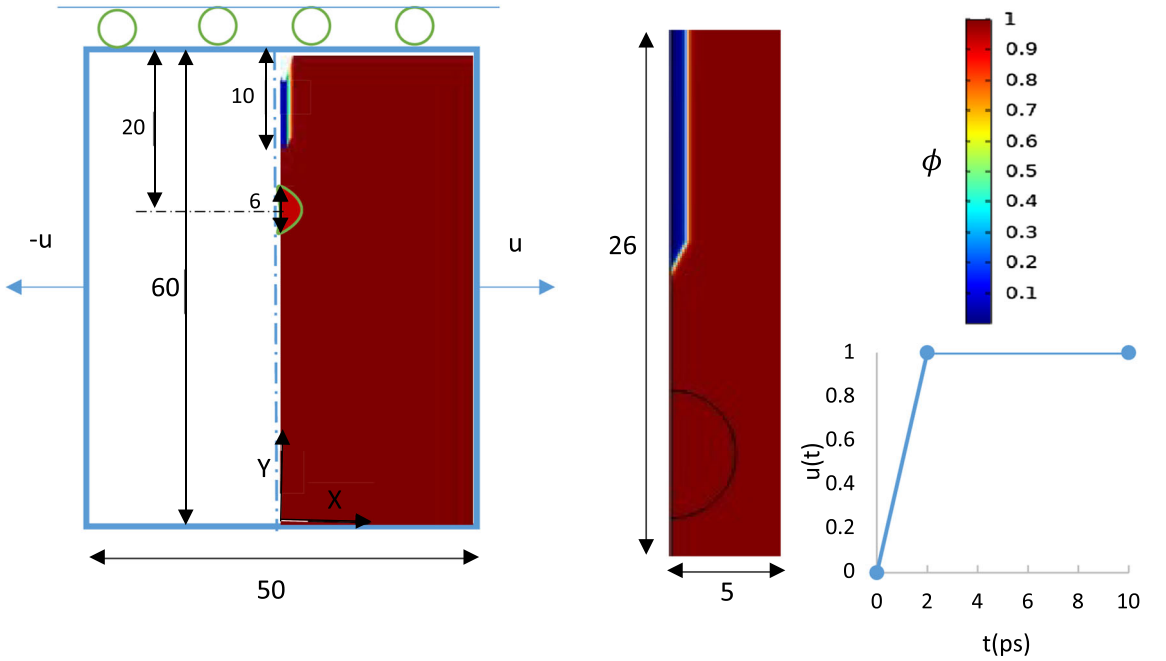


**Fig. 1** Schematics of the sample and loading

**Table 1** Initial matrix and particle properties

| Parameters | Notation | Value |
|---|---|---|
| Elastic modules of matrix | $E_{0m}$ | 50 GPa |
| Elastic modules of particle | $E_{0p}$ | 50 GPa |
| Surface energy of matrix | $\gamma_m$ | 1.5N/m |
| Surface energy of particle | $\gamma_p$ | 1N/m |
| Kinetic coefficient factor | $L$ | 250(Pa.s)$^{-1}$ |
| Gas state elastic modules | $\zeta$ | $1e^{-4}$ |
| Matrix's Poisson's ratio | $\nu_m$ | 0.238 |
| Particle's Poisson's ratio | $\nu_p$ | 0.3 |
| The value of surface width | $\omega$ | 0.075nm |

investigated further. This very small value in this problem is equal to $\zeta \boldsymbol{C}_0$, unless stated otherwise. Therefore, degradation function is updated into Eq. 23:

$$I(\phi) = (1-\zeta)\left(4\phi^3 - 3\phi^4\right) + \zeta \tag{23}$$

Obviously, the smaller $\zeta$ parameter is more physical. Critical loading is investigated by assuming various parameters of $\zeta$ Fig. 2.

A relatively high error rate (about 27%) is added to the critical loading by assuming gas elastic modulus coefficient up to 0.001, but by reducing the gas elastic modulus coefficient to 0.0001, this error reaches about two percent. By reducing the amount of error in critical loading and convergence of the problem in the gas elastic modulus coefficient of 0.0001 GPa, assumption of a very small elastic energy can be considered acceptable the numerical problem due to the small amount of error.

### 3.1 Elastic modulus effect of circular particle

To investigate the effects of elastic modulus on the crack growth, crack path, and stresses, all parameters of the matrix properties and circular particle are assumed to be equal in the problem formulation. Only the elastic modulus of the circular particles is varied, with values of 50, 100, 150, 200, and 250 GPa. The crack growth is observed at standard time intervals in the preceding sections.

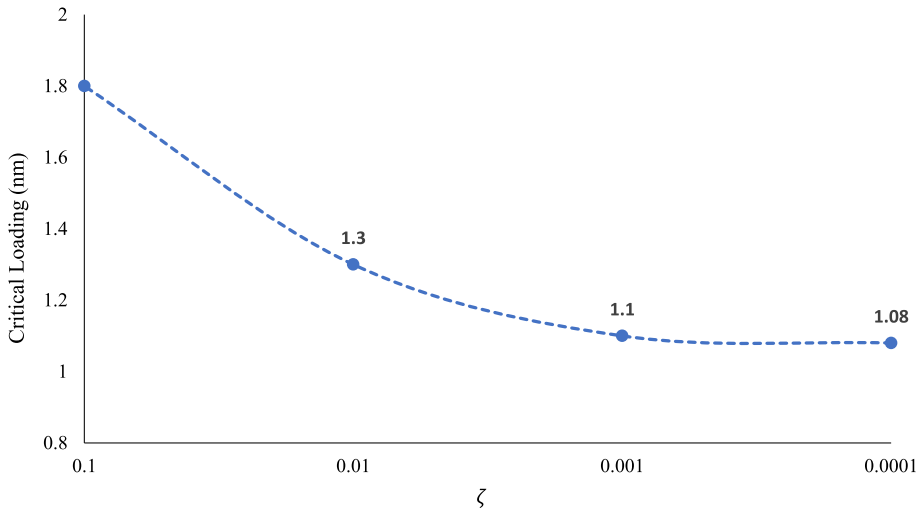


**Fig. 2** gas state elastic moduli coefficient effect ($\zeta$) on critical loading

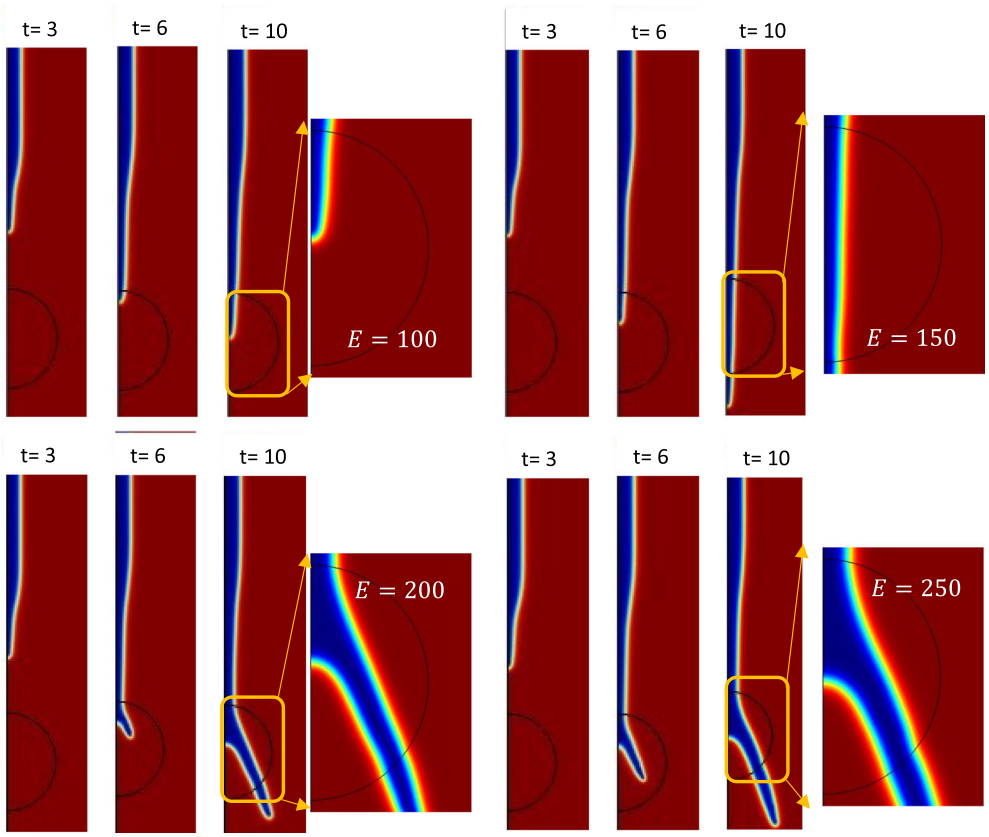


**Fig. 3** Elastic moduli effect on crack evolution

As shown in Fig. 3, for moduli less than 150 GPa (less than matrix moduli), the crack growth chooses the direct path through the composite just like neglecting the particle to put it differently; crack growth follows a direct path through the composite particle due to low energy absorption in the composite region. However, for moduli equal to or greater than 150 GPa, the crack growth deviates from within the composite particle, and after passing through the particle, the crack opening displacement in the specimen increases again.

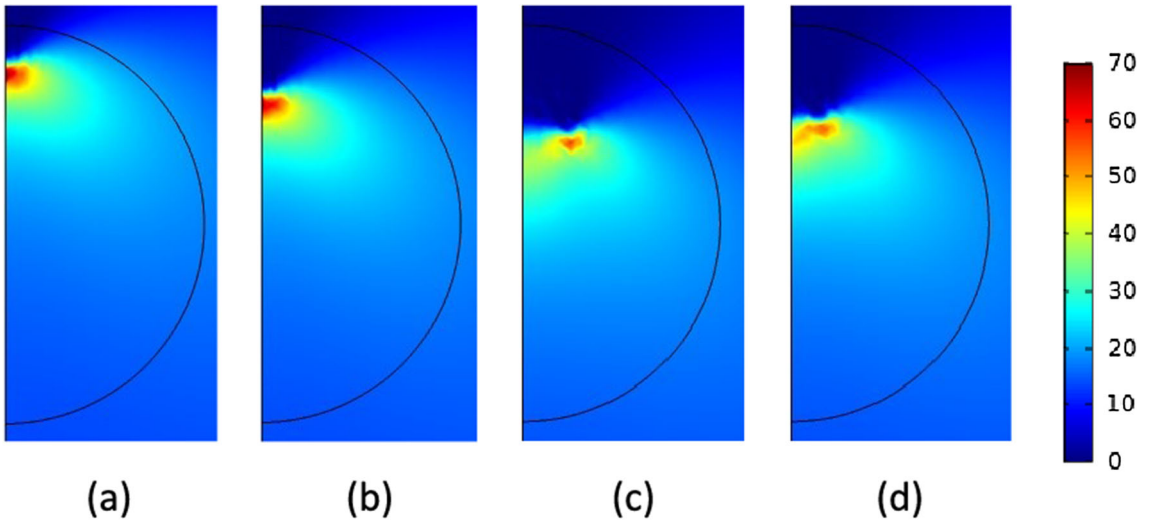


**Fig. 4** The horizontal stress field when the crack meets the particle with elastic modulus of **a** 100, **b** 150, **c** 200, **d** 250 GPa

Determining the stress field around the particle when the crack reaches the particle can provide justification for the crack path. For this purpose, the moment of crack-particle collision is obtained for each of the specimens, and the two-dimensional stress contour is shown in Fig. 4.

As clearly observed in Fig. 4, when the crack passes through the interior of the circular particle which has the elastic of 100 GPa, the stress field around the crack tip is confined, and this stress field is observed within a maximum radius of 2 nm. However, in elastic moduli of 200 and 250 GPa, the stress field is more extensive and continues up to 5 nm.

### 3.2 Surface energy effect of circular particle

In the phase-field equations, one of the important influential parameters in solving the phase-field function is the surface energy of the material ($\gamma$). In this study, the maximum value of the surface energy is assumed to be 3. To investigate the effect of this parameter, selected ranges for the surface energy parameter are defined as 1, 1.5, 2, 2.5, and 3 N/m, and the crack growth behavior in the nanocomposite particle is examined for each of these values.

Hence, the crack growth behavior in the nanocomposite particle is observed to vary with changes in the surface energy. Figure 5 illustrates the crack growth at different time intervals for varying values $\gamma$.

Thus, the surface energy of the nano-particles, similar to the elastic modulus, will also have a significant influence on the velocity and manner of crack growth. It is evident that with the elastic modulus considered for the circular particle in this case (50 GPa), the crack does not pass through the particle, and its path changes to bypass the circular particle for surface energy coefficients of 2, 2.5, and 3.

It appears that both the elastic modulus and the surface energy coefficient affect the manner and speed of crack growth. However, the extent of their influence may vary, and each parameter may have a greater or lesser role in crack propagation. If the effect of these two coefficients is considered in the total energy for crack growth, by taking into account the energy equation in Eq. 18, the coefficients $\gamma$ and $C_0$ can be deemed influential in the total energy and, ultimately, crack growth.

By modifying Eq. 20, the total energy can be regarded as a linear combination of the elastic modulus and the surface energy as below:

$$\Psi = X(\Phi, [\varepsilon])C_0 + Y(\Phi, |\nabla\Phi|)\gamma. \tag{24}$$

Indeed, the energy equation of Ginzburg-Landau does not explicitly capture the coupling between elastic modulus and surface energy, and it is not straightforward to make a definitive statement about the greater impact of either parameter.

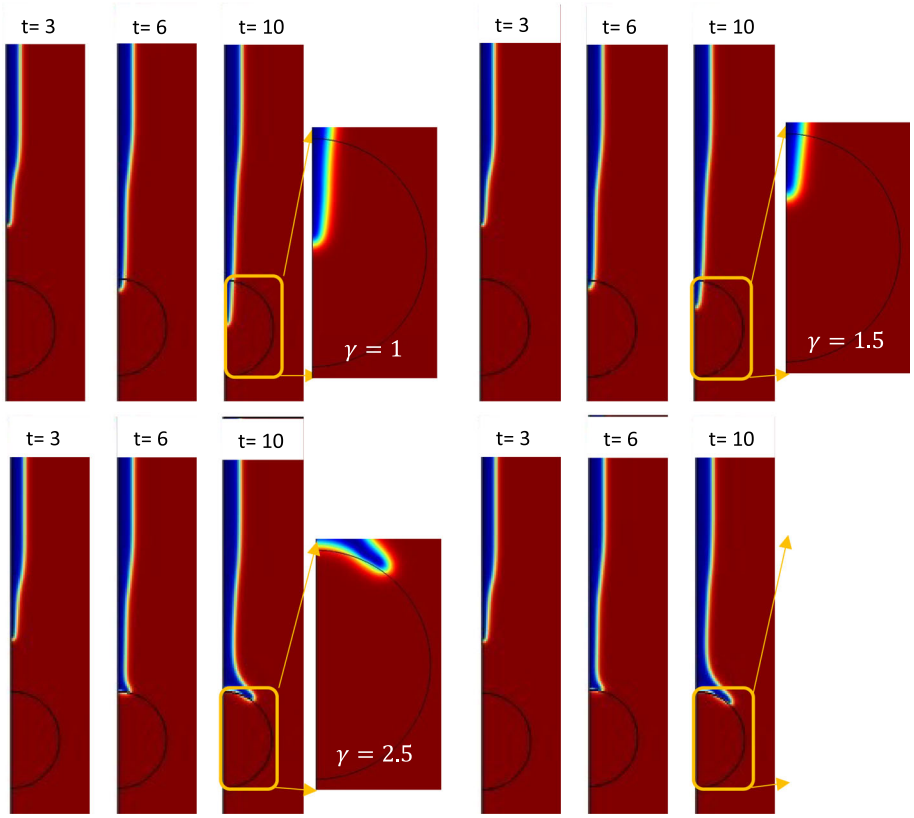


**Fig. 5** Effect of the surface energy value on crack propagation

### 3.3 Random nano-particle distribution

In the previous section, the behavior of crack propagation in a material using the phase-field method is investigated. The phase-field approach represents the crack as a diffuse interface characterized by a continuous variable. This variable describes the local state of the material, indicating whether it is intact or damaged.

In this study, the phase-field method is employed to simulate crack propagation and its interaction with particles in a composite material. The particles are assumed to have a circular shape with a diameter of 3 nm, and their distribution in the matrix is considered to be non-uniform.

The simulation results show that the particles have a significant effect on the crack propagation behavior. They act as obstacles, causing the crack to deviate from its straight path and creating stress concentrations around them. Moreover, the interaction between the crack and particles leads to crack branching and changes in its propagation direction.

By considering the non-uniform distribution of particles and their effects on crack behavior, a more realistic representation of crack propagation in composite materials can be achieved. This understanding can contribute to the design and optimization of materials with improved fracture resistance. For example, in the case of a nanocomposite material, a uniform distribution of nanoparticles with a diameter of 3 nm can be assumed in the matrix. In this distribution, the nanoparticles are randomly positioned within the matrix [63]. Thus, by considering this assumption, the distribution of circular particles with a size of 3 nm and a non-uniform arrangement in the background can be considered.

In the distribution of particles, the interactions between neighboring particles affect their arrangement. In these interactions, neighboring particles repel each other due to their overlapping and tend to achieve a minimum energy state. The angles between the vectors connecting the centers of neighboring particles also play a role in the arrangement of particles, causing variations in their positions and orientations.

Therefore, the understanding of the effects of particle arrangement and the angles between neighboring particles on crack behavior and fracture toughness in nanocomposite materials can be improved. This knowledge is important for designing and engineering materials with enhanced mechanical properties.

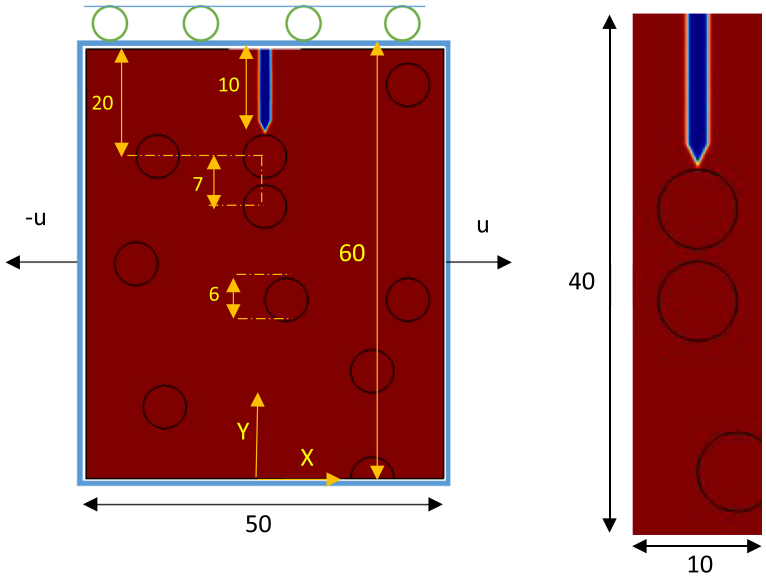


**Fig. 6** Crack schematic and particle arrangement in the sample

In this study, a spherical particle is deliberately placed in the path of crack growth, and other particles are created in a random way in the field of matter. The properties of the matrix were different with the spherical particles so that the effects of the crack passage on these properties could be determined. The change of properties from the matrix to spherical particles is assumed without the presence of an interphase layer.

A rectangular sample with dimensions of $60 \times 50$ nm$^2$ with a number of circular particles at different distances and a particle radius of 3 nm has been considered. The initial crack with a length of 10 nm is created at the top and in the middle of the sample. The assumption of plain strain has been taken into account in this problem and a time-dependent loading is applied symmetrically to the horizontal corners of the sample, as before. The total solution time is considered to be 10 ps and the problem is solved with 1000 equal time steps. Due to the geometry and asymmetric loading, unlike the previous problems, the entire sample is simulated. The mesh of the whole sample is selected in the form of a modified triangle with a minimum size of 0.018 nm. The elasticity and phase-field equations are solved in the form of a couple to reach the result. Figure 6 illustrates the schematic of the sample and the created initial crack.

In this problem, a matrix with the following properties is defined: bulk modulus $K_{\mathrm{m}} = 112.62$ GPa, shear modulus $G_{\mathrm{m}} = 71.5$ GPa, surface energy parameter $\gamma_{\mathrm{m}} = 1.5$ N/m, and characteristic crack thickness $\omega = 0.075$ nm. The matrix's kinetic coefficient parameter is chosen as $\mathrm{L} = 250\ (\mathrm{Pa.s})^{-1}$. The composite particles are assumed to have an elastic modulus $\mathrm{E_p} = 50$ GPa, surface energy parameter $\gamma_{\mathrm{p}} = 2.5$ N/m, and Poisson's ratio $\nu_{\mathrm{p}} = 0.3$. The applied loading in this case is $u = 1.5$ nm/ps. The elastic energy of the gas phase is negligible, and the primary crack function is defined as Eq. 29.

As observed in the previous section, crack growth depends on the mechanical properties of the circular particle. In this section, with the presence of non-uniform particle distribution, it appears that upon loading, the distance between particles affects the stress field around the crack and particles. The distance between particles can be divided into longitudinal and angular distances, and the effect of each can be examined separately. To simplify the problem, the distance between the closest particle to the crack passage is considered, and the impact of the size and angle of these distances is investigated.

### 3.4 Particle distance effect

In this configuration, the particle closest to the crack path has been selected to investigate and compare the crack growth and induced stresses by varying its distance from the initial position. The center distance of the closest particle from the crack path is initially 7 nm. By changing this longitudinal distance to 10, 14, and 30 nm while maintaining the angular position constant, the crack growth is examined. The crack state and horizontal stress at the end of the solution are presented in Fig. 7.

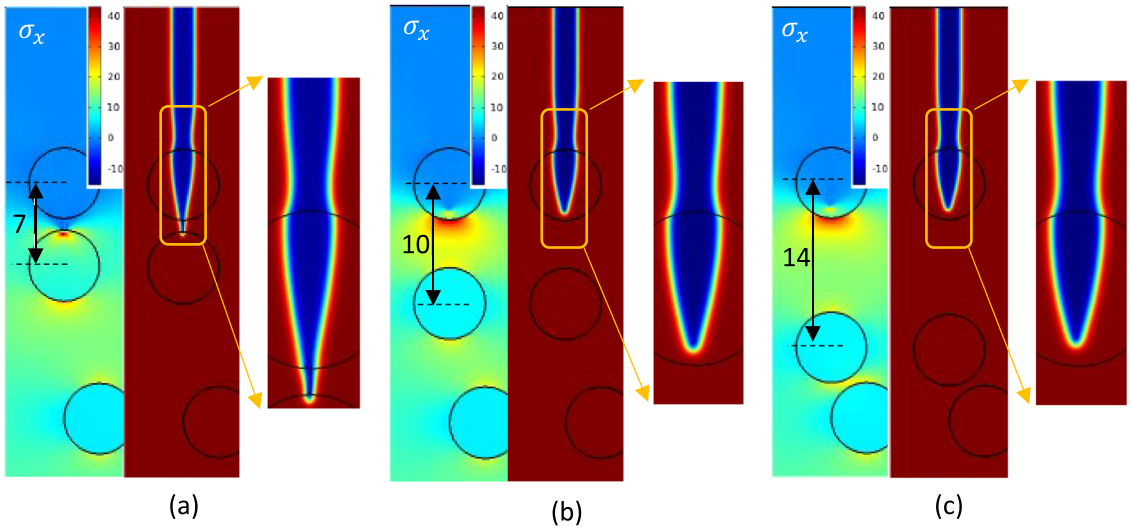


**Fig. 7** Crack evolution and horizontal stress at different particle location

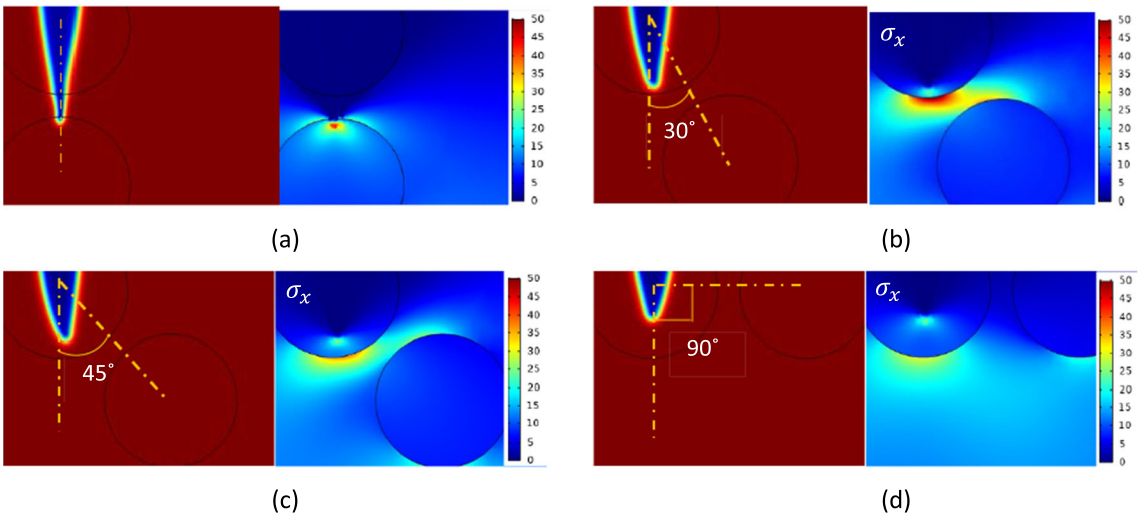


**Fig. 8** Schematic of the crack at 10 ps, with 7 nm distance between two particles and **a** zero, **b** 30, **c** 45 and **d** 90 degree angular positions

As anticipated, the crack growth depends on the distances between the composite particles, which is attributed to the significant stress field generated in the composite particles and the crack profile. Additionally, particles located in the vicinity of the crack path appear to have a significant influence on crack growth. This is demonstrated in Fig. 7, where the particle at a distance of 7 nm from the crack path causes the crack to propagate beyond the initial crack and reach the second particle. However, increasing the distance between the two particles does not result in any noticeable change in crack growth.

### 3.5 Particle angular positioning effect

In addition to the distance parameter, the angular position of the particles can also play a significant role in crack growth. Therefore, in this section, a reference distance of 7 nm is chosen between the two selected particles, and the angular position of the second particle relative to the crack path is varied. The variations in angular position at angles of 0, 30, 45, and 90 degrees are selected. Figure 8 illustrates the crack state at the end of the problem-solving process for the aforementioned angular positions.

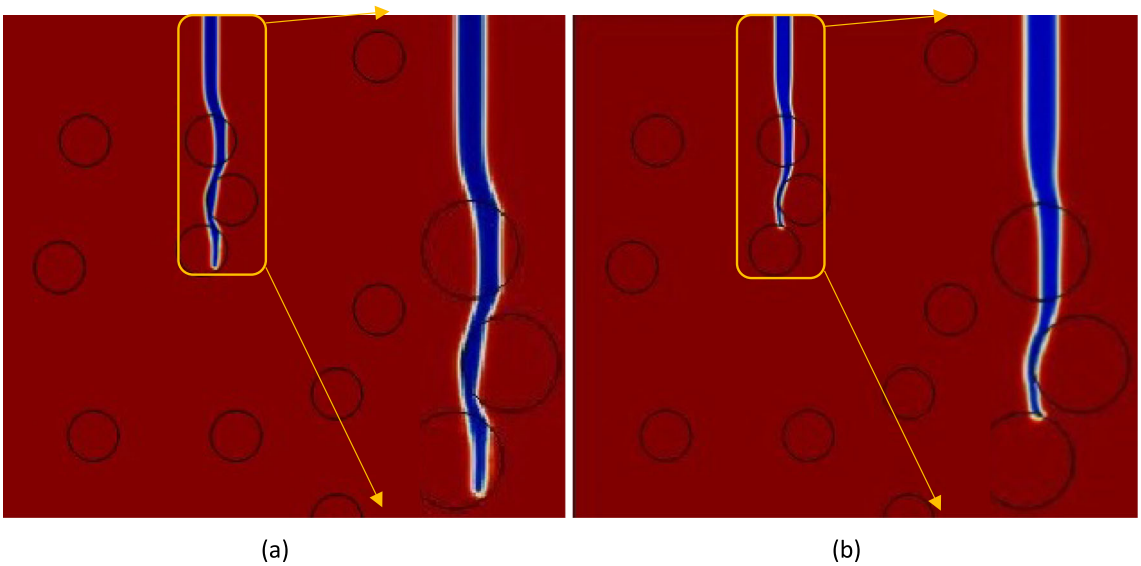


**Fig. 9** Crack evolution in a 10% distorted distribution **a** with, **b** without surface tension effect

The angular position, similar to the longitudinal distance, also has an impact on effective crack growth, as the crack tip is attracted toward the position of the nearest particle, acting like a magnet. If the particle is aligned with the crack growth direction, this effect promotes crack growth. As the angular position between the particle and the crack path increases, the crack tip is deflected toward the center of the particle. This continues until the angle between the two particles reaches 90 degrees, or in other words, when the angle of crack growth becomes perpendicular to the centers of the two particles. In this case, presence of this particle acts as a brake against crack growth and has the most significant influence in preventing crack propagation.

The reason behind this phenomenon can be investigated in terms of the stress field generated, similar to the longitudinal distance. The change in particle position will indeed result in a change in the stress field. The closer the particle is to the crack growth direction and to the crack tip, the higher the generated stress level will be. Consequently, the crack growth will be more influenced by these factors, as the increased stress level promotes crack propagation.

### 3.6 Surface tension effect

In the presented results so far, the influence of each factor on crack growth has been examined, and the extent of the effect of changing each of these factors has been determined. To summarize and observe the interactions of these factors and the types of crack interactions with a circular particle (stopping, passing through, and bypassing the particle), a nanocomposite sample with 10% volume fraction of circular particles is considered. The elastic modulus of the particles in this problem is assumed to be $E_{\mathrm{p}} = 250$ GPa, and all initial conditions, loading, and material properties are taken similar to previous section.

As shown in Fig. 9, the crack defined under these specified conditions encounters the first particle and passes through it, but during the passage, it gets deflected toward the second crack. Since the modulus of the particles is higher than the assumed background modulus, the crack bypasses this particle and ultimately reaches the third particle, where it comes to a halt. In the case where surface stresses are not considered, it was possible to solve the problem until 15 ps, and the crack growth could occur to a greater extent. Figure 9 illustrates the state of crack growth at the end of the problem solution. In this case, it is evident that the third particle is also bypassed by the crack.

## 4 Conclusion

In this study, simulation of crack in the nanoscale was conducted step by step, with the aim of simulating a nanocomposite materials. A double-well energy potential function is considered in this problem, which has

advantages and disadvantages. Indeed, the presence of the double-well potential function did not pose any issues in the solution process. All derived equations and the implemented code in the COMSOL software, as detailed in Chapter 2, are thermodynamically based. Therefore, the results obtained from the numerical solution of these finite element problems are thermodynamically consistent.

In reality, the elastic energy of the gas phase should be defined as zero. However, to prevent numerical inconsistencies, a very small value was assigned to it. The presence of additional elastic energy in the general case leads to an increase in critical loading. Considering the numerical solution process, the smallest definable value with a partial error of two percent was defined as 0.0001 GPa.

The presence of a circular particle in the specimen affects the path and velocity of crack growth. The growth, stoppage, or change in the crack's path upon encountering the circular particle depend on the elastic modulus and the surface energy coefficient of particle and matrix. In lower or equal modulus values compared to the elastic modulus of the matrix, the crack continues to grow by passing through the circular particle. However, in higher modulus values, the crack's path is altered and tends to bypass the circular particle. Similar results were observed for the surface energy coefficient of the circular particle, where an increase in the coefficient led the crack to deviate from its initial path and bypass the particle. With a 30% increase in the surface energy coefficient of particle compared to the matrix, the crack growth was almost prevented, and with a 60% and 100% increase, the crack started to bypass the particle.

**Acknowledgements** The support of the Isfahan University of Technology and Iran National Science Foundation is gratefully acknowledged.

**Author contributions** M.M. was contributed to software, validation, formal analysis, writing—original draft, data curation, visualization M. J. was contributed to conceptualization, methodology, software, formal analysis, writing—original draft, writing—review and editing, supervision, project administration, funding acquisition H.J. was contributed to methodology, software, formal analysis, writing—original draft, writing—review and editing

**Declarations**

**Competing interests** The authors declare no competing interests.

## References

1. Aranson, I., Kalatsky, V., Vinokur, V.: Continuum field description of crack propagation. Phys. Rev. Lett. **85**(1), 118 (2000)
2. Karma, A., Kessler, D.A., Levine, H.: Phase-field model of mode III dynamic fracture. Phys. Rev. Lett. **87**(4), 045501 (2001)
3. Jafarzadeh, H., Mansoori, H.: Phase field approach to mode-I fracture by introducing an eigen strain tensor: general theory. Theoret. Appl. Fract. Mech. **108**, 102628 (2020)
4. Farrahi, G.H., Javanbakht, M., Jafarzadeh, H.: On the phase field modeling of crack growth and analytical treatment on the parameters. Continuum Mech. Thermodyn. **32**(3), 589–606 (2020)
5. Levitas, V.I., Jafarzadeh, H., Farrahi, G.H., Javanbakht, M.: Thermodynamically consistent and scale-dependent phase field approach for crack propagation allowing for surface stresses. Int. J. Plast. **111**, 1–35 (2018)
6. Steinbach, I.: Phase-field models in materials science. Model. Simul. Mater. Sci. Eng. **7**, 073001 (2009).
7. Artemev, A., Jin, Y., Khachaturyan, A.: Three-dimensional phase field model of proper martensitic transformation. Acta Mater. **49**(7), 1165–1177 (2001)
8. Javanbakht, M., Rahbar, H., Ashourian, M.: Explicit nonlinear finite element approach to the Lagrangian-based coupled phase field and elasticity equations for nanoscale thermal-and stress-induced martensitic transformations. Contin. Mech. Thermodyn. 1–20 (2020)
9. Levitas, V.I., Javanbakht, M.: Phase-field approach to martensitic phase transformations: effect of martensite–martensite interface energy. Int. J. Mater. Res. **102**(6), 652–665 (2011)
10. Seol, D., et al.: Cubic to tetragonal martensitic transformation in a thin film elastically constrained by a substrate. Met. Mater. Int. **9**, 221–226 (2003)
11. Chen, L.-Q.: Phase-field models for microstructure evolution. Annu. Rev. Mater. Res. **32**(1), 113–140 (2002)
12. Rahbar, H., et al.: Finite element analysis of coupled phase-field and thermoelasticity equations at large strains for martensitic phase transformations based on implicit and explicit time discretization schemes. Mech. Adv. Mater. Struct. **29**(17), 2531–2547 (2022)
13. Voyiadjis, G.Z., Mozaffari, N.: Nonlocal damage model using the phase field method: theory and applications. Int. J. Solids Struct. **50**(20–21), 3136–3151 (2013)
14. Duda, F.P., et al.: A phase-field/gradient damage model for brittle fracture in elastic–plastic solids. Int. J. Plast. **65**, 269–296 (2015)

15. Javanbakht, M., Levitas, V.I.: Phase field approach to dislocation evolution at large strains: computational aspects. Int. J. Solids Struct. **82**, 95–110 (2016)
16. Amirian, B., et al.: Phase-field approach to evolution and interaction of twins in single crystal magnesium. Comput. Mech. **70**(4), 803–818 (2022)
17. Jafarzadeh, H., Levitas, V. I., Farrahi, G. H., Javanbakht, M.: Phase field approach for nanoscale interactions between crack propagation and phase transformation. Nanoscale. **11**(46), 22243–22247 (2019)
18. Amirian, B., et al.: Thermodynamically-consistent derivation and computation of twinning and fracture in brittle materials by means of phase-field approaches in the finite element method. Int. J. Solids Struct. **252**, 111789 (2022)
19. Li, W., Landis, C.M.: Nucleation and growth of domains near crack tips in single crystal ferroelectrics. Eng. Fract. Mech. **78**(7), 1505–1513 (2011)
20. Zhao, T., Zhu, J., Luo, J.: Study of crack propagation behavior in single crystalline tetragonal zirconia with the phase field method. Eng. Fract. Mech. **159**, 155–173 (2016)
21. Jafarzadeh, H., Farrahi, G.H., Javanbakht, M.: Phase field modeling of crack growth with double-well potential including surface effects. Continuum Mech. Thermodyn. **32**, 913–925 (2020)
22. Jafarzadeh, H., et al.: Phase field theory for fracture at large strains including surface stresses. Int. J. Eng. Sci. **178**, 103732 (2022)
23. Henry, H., Levine, H.: Dynamic instabilities of fracture under biaxial strain using a phase field model. Phys. Rev. Lett. **93**(10), 105504 (2004)
24. Hakim, V., Karma, A.: Crack path prediction in anisotropic brittle materials. Phys. Rev. Lett. **95**(23), 235501 (2005)
25. Hakim, V., Karma, A.: Laws of crack motion and phase-field models of fracture. J. Mech. Phys. Solids **57**(2), 342–368 (2009)
26. Kakouris, E.G., Triantafyllou, S.P.: Material point method for crack propagation in anisotropic media: a phase field approach. Arch. Appl. Mech. **88**(1), 287–316 (2018)
27. Hansen-Dörr, A.C., Brummund, J., Kästner, M.: Phase-field modeling of fracture in heterogeneous materials: jump conditions, convergence and crack propagation. Arch. Appl. Mech. **91**(2), 579–596 (2021)
28. Miehe, C., Welschinger, F., Hofacker, M.: Thermodynamically consistent phase-field models of fracture: variational principles and multi-field FE implementations. Int. J. Numer. Methods Eng. **83**(10), 1273–1311 (2010)
29. Ambati, M., Gerasimov, T., De Lorenzis, L.: Phase-field modeling of ductile fracture. Comput. Mech. **55**, 1017–1040 (2015)
30. Griffith, A.A.: VI. The phenomena of rupture and flow in solids. In: Philosophical Transactions of the Royal Society of London. Series A, Containing Papers of a Mathematical or Physical Character. **221**(582–593), 163–198 (1921)
31. Amor, H., Marigo, J.-J., Maurini, C.: Regularized formulation of the variational brittle fracture with unilateral contact: Numerical experiments. J. Mech. Phys. Solids **57**(8), 1209–1229 (2009)
32. Miehe, C., Hofacker, M., Welschinger, F.: A phase field model for rate-independent crack propagation: robust algorithmic implementation based on operator splits. Comput. Methods Appl. Mech. Eng. **199**(45–48), 2765–2778 (2010)
33. Fang, J., et al.: Phase field fracture in elasto-plastic solids: a length-scale insensitive model for quasi-brittle materials. Comput. Mech. **66**(4), 931–961 (2020)
34. Ambati, M., Kruse, R., De Lorenzis, L.: A phase-field model for ductile fracture at finite strains and its experimental verification. Comput. Mech. **57**, 149–167 (2016)
35. Mesgarnejad, A., Imanian, A., Karma, A.: Phase-field models for fatigue crack growth. Theor. Appl. Fract. Mech. **103**, 102282 (2019)
36. Schreiber, C., Müller, R., Kuhn, C.: Phase field simulation of fatigue crack propagation under complex load situations. Arch. Appl. Mech. **91**(2), 563–577 (2021)
37. Seiler, M., et al.: Phase-field modelling for fatigue crack growth under laser shock peening-induced residual stresses. Arch. Appl. Mech. **91**(8), 3709–3723 (2021)
38. Liu, T., Long, R., Hui, C.-Y.: The energy release rate of a pressurized crack in soft elastic materials: effects of surface tension and large deformation. Soft Matter **10**(39), 7723–7729 (2014)
39. Porter, D.A., Easterling, K.E.: Phase Transformations in Metals and Alloys (revised reprint). CRC Press (2009).
40. Cammarata, R.C., Sieradzki, K.: Surface and interface stresses. Annu. Rev. Mater. Sci. **24**(1), 215–234 (1994)
41. Li, Y., Wang, G.-F.: Influence of surface tension on mixed-mode cracks. Int. J. Appl. Mech. **7**(05), 1550070 (2015)
42. Wang, G., Li, Y.: Influence of surface tension on mode-I crack tip field. Eng. Fract. Mech. **109**, 290–301 (2013)
43. Thomson, R., Chuang, T.-J., Lin, I.-H.: The role of surface stress in fracture. Acta Metall. **34**(6), 1133–1143 (1986)
44. Wu, C.H.: The effect of surface stress on the configurational equilibrium of voids and cracks. J. Mech. Phys. Solids **47**(12), 2469–2492 (1999)
45. Wang, G.-F., et al.: Surface effects on the near-tip stresses for mode-I and mode-III cracks (2008)
46. Fu, X., Wang, G., Feng, X.: Surface effects on mode-I crack tip fields: a numerical study. Eng. Fract. Mech. **77**(7), 1048–1057 (2010)
47. Fu, X., Wang, G., Feng, X.: Surface effects on the near-tip stress fields of a mode-II crack. Int. J. Fract. **151**(2), 95–106 (2008)
48. Kim, C., Schiavone, P., Ru, C.-Q.: Analysis of a mode-III crack in the presence of surface elasticity and a prescribed non-uniform surface traction. Z. Angew. Math. Phys. **61**, 555–564 (2010)
49. Camas, D., Garcia-Manrique, J., Gonzalez-Herrera, A.: Crack front curvature: Influence and effects on the crack tip fields in bi-dimensional specimens. Int. J. Fatigue **44**, 41–50 (2012)
50. Nguyen, V.-D., et al.: A large strain hyperelastic viscoelastic-viscoplastic-damage constitutive model based on a multi-mechanism non-local damage continuum for amorphous glassy polymers. Int. J. Solids Struct. **96**, 192–216 (2016)
51. Msekh, M.A., et al.: Predictions of J integral and tensile strength of clay/epoxy nanocomposites material using phase field model. Compos. B Eng. **93**, 97–114 (2016)
52. Msekh, M.A., et al.: Fracture properties prediction of clay/epoxy nanocomposites with interphase zones using a phase field model. Eng. Fract. Mech. **188**, 287–299 (2018)
53. Goswami, S., et al.: Transfer learning enhanced physics informed neural network for phase-field modeling of fracture. Theoret. Appl. Fract. Mech. **106**, 102447 (2020)

54. Goswami, S., Anitescu, C., Rabczuk, T.: Adaptive fourth-order phase field analysis using deep energy minimization. Theoret. Appl. Fract. Mech. **107**, 102527 (2020)
55. Yin, B., Kaliske, M.: Fracture simulation of viscoelastic polymers by the phase-field method. Comput. Mech. **65**, 293–309 (2020)
56. Brighenti, R., Rabczuk, T., Zhuang, X.: Phase field approach for simulating failure of viscoelastic elastomers. Eur J Mech-A/Solids **85**, 104092 (2021)
57. Loew, P.J., Peters, B., Beex, L.A.: Rate-dependent phase-field damage modeling of rubber and its experimental parameter identification. J. Mech. Phys. Solids **127**, 266–294 (2019)
58. Unger, R., et al.: Effect of temperature on the viscoelastic damage behaviour of nanoparticle/epoxy nanocomposites: constitutive modelling and experimental validation. Polymer **191**, 122265 (2020)
59. Henshell, R.D., Shaw, K.G.: Crack tip finite elements are unnecessary. Int. J. Numer. Methods Eng. **9**, 495–507 (1975)
60. Barsoum, R.S.: On the use of isoparametric finite elements in linear fracture mechanics. Int. J. Numer. Meth. Eng. **10**(1), 25–37 (1976)
61. Auricchio, F., et al.: Isogeometric collocation for elastostatics and explicit dynamics. Comput. Methods Appl. Mech. Eng. **249**, 2–14 (2012)
62. Dusane, A., et al.: Simulation of bridging mechanisms in complex laminates using a hybrid PF-CZM method. Mech. Adv. Mater. Struct. **29**(28), 7743–7771 (2022)
63. Jafarzadeh, H., Shchyglo, O., Steinbach, I.: Multi-phase-field approach to fracture demonstrating the role of solid-solid interface energy on crack propagation. Int. J. Fract. **245**, 75–87 (2024). https://doi.org/10.1007/s10704-024-00762-x